Available online at www.sciencedirect.com

ScienceDirect

International Journal of Machine Tools & Manufacture 47 (2007) 112–123

INTERNATIONAL JOURNAL OF MACHINE TOOLS & MANUFACTURE DESIGN, RESEARCH AND APPLICATION

www.elsevier.com/locate/ijmactool

Numerical simulation and experimental investigation of gas–powder flow from radially symmetrical nozzles in laser-based direct metal deposition

Srdja Zekovic, Rajeev Dwivedi, Radovan Kovacevic*

Research Center for Advanced Manufacturing, Southern Methodist University, 1500 International Parkway, Suite #100, Richardson TX-75081, USA

Received 19 December 2005; received in revised form 15 February 2006; accepted 17 February 2006

Abstract

Laser-based direct metal deposition (DMD) is a solid freeform fabrication process capable of fabricating fully dense and metallurgically sound parts. The process has been greatly enhanced toward multi-directional deposition by the use of discontinuous radially symmetrical powder nozzles to supply the build material. Since many operational parameters depend on the gas–powder stream characteristics between the nozzles and the deposition point, an extensive understanding of the gas–powder flow is necessary. Three-dimensional (3D) multi-phase gas–powder flow structures of radially symmetrical nozzles are modeled using computational fluid dynamics methods. The obtained results are in good agreement with the experimental ones, and they provide a good insight into the process phenomena.

Keywords: Numerical simulation; Gas–powder flow; Radially symmetrical nozzles; Laser metal deposition

---

1. Introduction

One of the most important goals in the modern manufacturing community is the reduction of the concept-to-production delay [1]. Research in this area has contributed to the growth of rapid prototyping (RP) and rapid tooling (RT) techniques, which is extended to the new concept of making functional parts, termed rapid manufacturing (RM) [2]. Also, some of these technologies have already been applied successfully in parts refurbishment and repair [3].

Several RP techniques allow the fabrication of fully dense and metallurgically sound metallic parts, suitable for functional testing and application. The techniques such as direct metal deposition (DMD), laser engineered net shaping (LENS^{TM}), and direct light fabrication (DLF) are able to use a three-dimensional (3D) CAD solid model to produce a part from materials such as tool steels, high alloy steels, nickel super alloys, etc. without intermediate steps. The processes use a high power laser focused onto a metal substrate to create a molten pool on the surface of the substrate. Metal powder is then injected into the molten pool to increase the material volume. The substrate is scanned relative to the deposition head in order to write lines of the metal with a finite width and thickness, making a layer of deposited material. Finally, this procedure is repeated many times, layer by layer, until the entire object, represented by the 3D CAD model, is produced on the machine.

A stable and repeatable layer manufacturing procedure is crucial for the quality of the part produced by laser metal deposition (such as the geometric accuracy, residual stress, microstructure, structural integrity, etc.) However, this method for metal parts building suffers more from instability and non-repeatability problems than other RP methods. In direct laser metal deposition, a number of parameters govern the process [4]. They are sensitive to the environmental variations, and they are also interdependent. The supply of the additive material is one of the key factors controlling the process. The powders used for laser cladding should have a particle size between 20 and

---

*Corresponding author. Tel.: +1 214 768 4865; fax: +1 214 768 0812.
E-mail address: kovacevi@engr.smu.edu (R. Kovacevic).

0890-6955/$ - see front matter © 2006 Elsevier Ltd. All rights reserved.
doi:10.1016/j.ijmachtools.2006.02.004

Nomenclature

a_1, a_2, a_3	constants
C_D	drag coefficient
C_1, C_2, C_μ	coefficients in turbulent transport equations
d	diameter (m)
E	element number
F_i	force (N)
F_D	drag force (N)
g	gravitational acceleration (m/s^2)
k	kinetic energy of turbulence (m^2/s^2)
n	number of particles
p	pressure (N/m^2)
Re	relative Reynolds number
Pr	Prandtl number
t	time (s)
u	gas flow velocity (m/s)
$\bar{u}$	gas flow mean velocity vector (m/s)
u'	gas flow velocity vector fluctuation (m/s)
u^p	particle velocity (m/s)
u_o	optics protective gas velocity (m/s)
u_c	carrier gas–powder velocity (m/s)
V	volume (m^3)
x	Cartesian coordinate (m)

Greek letters

ε	rate of dissipation of turbulence energy (m^2/s^3)
Φ^M	source term (kg/m^2 s^2)
η	number of particles per unit time
μ	dynamic viscosity (kg/s m)
ρ	density (kg/m^3)
σ_k	turbulent Prandtl number for k
σ_ε	turbulent Prandtl number for ε

Subscripts

i, j	Cartesian coordinate directions
p	particle
t	turbulent flow
C	cell

200 μm. The best feeding properties are achieved with a spherical form of the particles, typical for atomized powders.

There are three different concepts of powder injection: off-axis powder injection (a single powder stream is fed laterally into the laser beam), continuous coaxial powder injection (a powder stream cone is produced that encloses the laser beam), and discontinuous coaxial powder injection (three or more powder streams are fed coaxially to the laser beam). The off-axis powder injection nozzle is suited only for 2D applications, because the clad track depends on the scan direction. Applications for the coaxial powder injection nozzle are 2D and 3D part reconditioning processes since many of the parts (e.g. airfoil tips) require small tracks. The major advantage of the discontinuous coaxial powder injection is the potential to tilt the deposition head without influencing the powder stream. This feature allows multi-axis deposition [5].

The multi-fabrication (MultiFab) system based on the combination of additive (laser metal deposition and arc welding) and subtractive (milling, drilling, and turning) techniques developed at Southern Methodist University is a promising manufacturing system that can be widely applied in solid freeform fabrication (SFF), functionally graded materials (FGM) deposition, component repair, and surface modification [6].

The MutiFab system exploits the multi-axis additive blown-powder laser-based direct metal deposition (LBDMD) process for the near-net fabrication of fully dense small and intricate features of metallic prototypes by a layered manufacturing method. Since the additive material is in the form of powder, the powder delivery subsystem that consists of powder feeders and a radially symmetrical nozzles setup plays a very important role in the process.

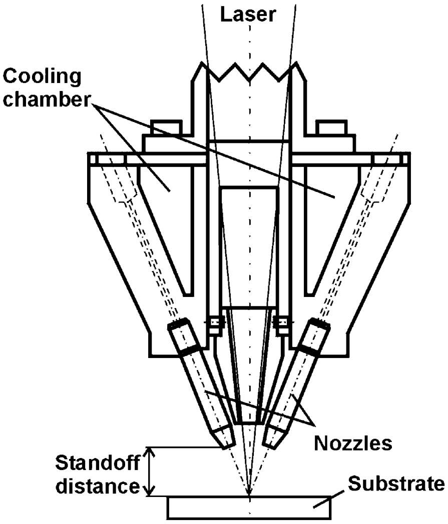

Fig. 1. The nozzle setup of the powder delivery system.

The nozzles' setup, as a part of the laser deposition head, is the key component of the powder delivery system. A proper nozzle design allows the cladding process to be completed in a single step. Fig. 1 shows one type of nozzle setup applied in the powder delivery system. The deposition head provides laser light, powder, and protection gas. The powder, carried by the inert gas through four radially symmetrical nozzles at 30° to the vertical axis, is injected into the molten pool created by the laser beam. The powder feed rate ranges from 0.3 g/min to 50 g/min as governed by the rotational speed of the powder feeder rotating discs [7].

The inert gas also provides oxidation protection to the molten material and to the heat affected surrounding area. Due to the size of the powder (20–200 μm), and the relatively slight interaction between the laser and powder particles before they reach the molten pool, the powder particles are considered to remain solid until they enter the molten pool. Assuming the laser can provide enough energy, all particles that reach the molten pool are melted and fused to the substrate; whereas, the others ricochet and are lost. By controlling the laser power, scanning velocity, and powder flow rate; the deposited beads can be produced with different widths (1–2.5 mm) and heights (0.1–0.6 mm). In comparison with the two-stage laser sintering process, in which a powder is spread on the substrate before sintering, the direct laser deposition process does not require an inert-gas protection chamber. Larger parts can be produced, and more complex deposited paths (up to five-axis) can be traced. By controlling the mixing process of the powders from several powder feeders, a composite material with a functionally graded composition can be produced.

In addition to the set of the powder feeding nozzles, there is a coaxial nozzle in the center of the deposition head. The purpose of the coaxial nozzle, through which the laser beam is brought, is to direct an additional (secondary) inert gas stream toward the molten pool in order to prevent the ricocheted particles and the fumes from the molten pool from reaching and damaging the optics for laser beam shaping in the deposition head.

The powder particles are injected from the feeding system through cylindrical inlets to the four powder feeding nozzles. Traveling along the nozzles, particles collide with the nozzle walls. These collisions determine the concentration distribution and dispersion of the particles. After exiting the nozzles, the powder particles are drawn downward by the action of three factors: gravity, momentum from the transport gas, and momentum from the secondary gas flow. They then form one gas–powder stream directed to the molten pool.

The time and the spatial characteristics of the interaction between the powder and the laser beam are critical for the process. The physical properties of the powder material, the nature of the gas, the gas mass-flow rate, the stream spatial distribution, the particle size distribution, and the laser beam shape are among the parameters that are involved [4].

The shape of the gas–powder stream, combined with the size of the molten pool, have a large influence on the size and shape of the buildup, as well as on the powder efficiency; they determine the geometrical accuracy and the surface quality of the buildup. The shape of the gas–powder stream is tailored by the nozzle geometry, which means by the angle with respect to the vertical axis, by the vertical distance from the molten pool (or standoff distance), and by the gas velocity from the primary and secondary flows. Fearon et al. [8] investigated the effects of altering the configuration of a four-port nozzle system on the shape of the emitted powder streams. The possibility of depositing with a consistent layer height by controlling the powder efficiency in the vertical plane was demonstrated.

Also, some side effects such as blob formation on the nozzles during the deposition on flat substrates at high laser power can be observed. This phenomenon is a consequence of the interaction between the hot nozzle tips exposed to the reflected laser beam and the particles ricocheted from the substrate. The number and trajectories of the ricocheted particles depend on the gas–powder stream shape and the size of the molten pool.

As many operational parameters depend on the gas–powder stream characteristics between the nozzles and the deposition point, an extensive understanding of the powder stream properties, such as the concentration of the powder and the velocities of the gas and the powder particles will be helpful in determining the optimal operational parameters. Some experimental work has already been done, and the results have been incorporated in several mathematical models for the powder flow from the lateral nozzles and from the coaxial nozzles [9,10]. Given the complexity of the multiphase flow from any kind of nozzle, it is difficult to model analytically, so a precise simulation of the flow structure is generally regarded as requiring numerical modeling techniques [11].

Using a finite difference numerical algorithm based on a specific control-volume approach, the powder flow structures of a coaxial nozzle with various arrangements of the nozzle exit for laser cladding have been simulated [12]. A 2D axially symmetrical model of the two-phase turbulent gas–powder flow was used to investigate the influence of the nozzle arrangement and gas flow settings on the powder concentration in the stream.

Also, a 2D numerical discrete phase simulation has been developed to study the effects of the coaxial nozzle converging angle and the gas settings (inner/outer gas stream relation) on the powder stream structure [13]. The particle path based on the coupled particle–gas interactions in the two-phase turbulent flow was predicted using stochastic tracking.

In order to simulate and study powder flow behavior involved in the MultiFab's powder feeding system, a 3D model of the turbulent gas–powder flow, based on the nozzle setup shown in Fig. 1, has been developed. FLUENT software, based on a finite-volume approach, is used to perform a detailed numerical analysis of the powder stream without laser radiation. Since the gas–powder flow is characterized by the turbulence, and turbulence in turn is a 3D phenomenon, a 3D model is required. The model is used to gain full insight into the process and to analyze the influence of the processing parameters such as the standoff distance, volumetric gas flow rate, and mass flow rate on the output of the LBDMD process. Also, the developed model provides important parameters for the calculation of the heat transfer boundary conditions for the finite element model (FEM) of the LBDMD process

[14]. The three cases of the gas–powder flow are analyzed: (a) the laser head is far from the substrate, (b) the laser head is close to the flat substrate during deposition, and (c) the laser head is close to the top of the thin-walled buildup.

2. Numerical study of gas and powder turbulent flow

2.1. Modeling of turbulent flow

A significant property of the turbulent jet flow is that momentum, heat, and mass are transferred across the flow at rates much greater than those of the laminar flow with molecular transport processes by viscosity and diffusion. The numerical simulation of a turbulent flow involves the modification of the governing equations for the case of the laminar flow using a time-averaging procedure known as Reynolds averaging [15]. For a turbulent flow being steady, incompressible, isothermal, chemically homogeneous, and without body forces, the following equations apply:

Conservation of mass:

$$\frac{\partial \bar{u}_i}{\partial x_i} = 0. \tag{1}$$

Conservation of mean momentum (Navier–Stokes):

$$\frac{\partial}{\partial x_i}(\rho \bar{u}_j \bar{u}_i) + \frac{\partial}{\partial x_j}(\rho \overline{u'_i u'_i}) = -\frac{\partial \bar{p}}{\partial x_i} + \frac{\partial}{\partial x_j}\left[\mu\left(\frac{\partial \bar{u}_i}{\partial x_j} + \frac{\partial \bar{u}_j}{\partial x_i}\right)\right], \tag{2}$$

where $i, j = 1, 2, 3$, $\bar{u}_i$ is the mean velocity vector in the ith direction, p is the pressure, μ is the dynamic viscosity, ρ is the density, and $\rho\overline{u'_i u'_i}$ is the Reynolds stress. These equations can be solved for the mean values of velocity and pressure only if equations for the higher order correlations, e.g., for the Reynolds stress tensor, can be derived in some way. Therefore, turbulent modeling is the task of providing additional equations to describe the temporal and spatial evolution of the turbulent inertia flux.

The most popular turbulence model in practical use is the so-called two-equation model, or k-ε model. In the k-ε turbulent model, the turbulence field is characterized in terms of two variables, the turbulent kinetic energy k, and the viscous dissipation rate of turbulent kinetic energy ε. Two transport equations for k and ε can be obtained from the Navier–Stokes equations by a sequence of algebraic manipulations. Simplifying these two equations by using a number of modeling assumptions, the well-known equations of turbulent kinetic energy and dissipation of the k-ε model can be obtained [16].

Conservation of the kinetic energy of turbulence:

$$\frac{\partial}{\partial x_j}(\rho \bar{u}_j k) = \frac{\partial}{\partial x_j}\left(\frac{\mu_t}{\sigma_k}\frac{\partial k}{\partial x_j}\right) + G_k + G_b - \rho\varepsilon. \tag{3}$$

Conservation of the dissipation of kinetic energy of turbulence:

$$\frac{\partial}{\partial x_j}(\rho \bar{u}_j \varepsilon) = \frac{\partial}{\partial x_j}\left(\frac{\mu_t}{\sigma_\varepsilon}\frac{\partial \varepsilon}{\partial x_j}\right) + C_1\frac{\varepsilon}{k}(G_k + G_b) - C_2\rho\frac{\varepsilon^2}{k}, \tag{4}$$

$$G_k = \mu_t \frac{\partial \bar{u}_i}{\partial x_j}\left(\frac{\partial \bar{u}_i}{\partial x_j} + \frac{\partial \bar{u}_j}{\partial x_i}\right), \tag{5}$$

$$G_b = -g_i \frac{\mu_t}{\rho\, Pr_t}\frac{\partial \rho}{\partial x_i}, \tag{6}$$

where $i, j = 1,2,3$, $\mu = \mu_0 + \mu_t$ (μ_0—molecular viscosity, μ_t—turbulent viscosity), and $\mu_t = \rho C_\mu k^2/\varepsilon$, as proposed by Kolmogorov–Prandtl.

The above equations contain the empirical constants C_1, C_2, σ_k, σ_ε and C_μ. Over the years, the k-ε model has been tested and optimized for a wide range of flow problems. For the turbulent flow inside the nozzle, the following values of these empirical constants are selected: $C_1 = 1.44$, $C_2 = 1.92$, $\sigma_k = 1.00$, $\sigma_\varepsilon = 1.30$ and $C_\mu = 0.09$. G_k and G_b represent the rate of production of kinetic energy and the generation of turbulence due to buoyancy, respectively, while Pr_t is the turbulent Prandtl number for energy.

2.2. Near-wall modeling

The standard k-ε turbulence model is valid mostly for flows with a high Reynolds number. In a problem involving a solid boundary, there is always a special viscosity-affected near the wall region, which contains the viscous sub-layers. Therefore, a problem arises when an attempt is made to apply the standard k-ε turbulence model to a near-wall region. Thus, a special modeling approach is needed to simulate a turbulent flow in a near-wall region. In order to resolve the sharp variations of flow variables in near-wall regions, a prohibitively large number of grid points must be used, which leads to expensive computation. There are two approaches to model the near wall region. In the so-called wall-function approach, a set of special semi-empirical formulas are used to bridge the viscosity-affected region between the wall and the fully turbulent region. Another approach, the "near wall modeling" technique, uses the modified turbulence models in the viscosity-affected region, and they are resolved with a mesh all the way to the wall. In this study, the standard wall-function approach is used to overcome the viscosity-affected regions of the flow [17].

3. Modeling of two-phase flow

As it is pointed out, the flow in the nozzles and in the first interaction zone between the nozzles and the substrate is not a simple one-phase turbulent flow. Instead, this flow can, at best, be approximated as a two-phase flow, where the primary phase is the inert gas, and the secondary phase consists of the powder particles mixed with the gas.

Gas-particle flows are characterized by coupling between phases. The coupling through heat transfer from the gas phase to the particle phase and the momentum change, responsible for particle motion due to the aerodynamic drag, need to be incorporated in the numerical flow model. The behavior of particles suspended in a turbulent flow depends on the properties of both the particles and the flow. Turbulent dispersion of both the particles and the carrier gas can be handled by the concept of eddy diffusion energy in some range of the particle size distribution. The momentum transfer resulting from the interaction of the two phases has been investigated, and many criteria have been proposed. Because of the computation complexity of the particle and gas flow, many techniques have been proposed, but the uncertainty of the prediction model is still large [18,19].

In order to define the properties of a gas–particle mixture, the analyzed volume must be large enough to contain sufficient particles for a stationary average. Thus, the particles cannot be treated as a continuum in a flow system of comparable dimensions. The use of differential equations to relate particle cloud (and mixture) property changes through the application of the conservation equations is cautioned in this situation [20].

3.1. Dispersed phase modeling

In this study, the Lagrangian approach for two-phase flow modeling is used to model the powder particle mixing process. The underlying concept here is what is usually called the dispersed two-phase flow. The idea is to consider one of the phases (powder particles) to be dispersed in the other one (gas stream). At the same time, a strong coupling occurs between phases. The Lagrangian model represents the dispersed phase as a continuous stream of particles moving through the carrier phase. The governing equations for the carrier phase are given in the standard fluid dynamics Eulerian frame of reference, while the motion of the particles is described in a Lagrangian coordinate system. The information transfer between phases is accounted for by the momentum along the particle paths.

The motion of each particle of the dispersed phase is governed by an equation that balances the mass-acceleration of the particles with the forces acting on it. For a particle of density ρ_p and diameter d_p the governing equation is

$$\frac{\mathrm{d}u_i^\mathrm{p}}{\mathrm{d}t} = F_\mathrm{D}(u_i - u_i^\mathrm{p}) + \frac{(\rho_\mathrm{p} - \rho)}{\rho_\mathrm{p}} g_i + F_i, \tag{7}$$

where $i = 1, 2, 3$, u_i^p is the particle velocity, and μ_i is the velocity of the carrier phase. The first term on the right-hand side of Eq. (7) is the drag force per unit particle mass defined by

$$F_\mathrm{D} = \frac{18\mu}{\rho_\mathrm{p} d_\mathrm{p}^2} \frac{C_\mathrm{D}\, Re}{24}, \tag{8}$$

where μ is the fluid phase dynamic viscosity, and Re is the relative Reynolds number defined by

$$Re = \frac{\rho d_\mathrm{p} |u_i - u_i^\mathrm{p}|}{\mu} \tag{9}$$

and C_D is the drag coefficient. There exist many models to determine the drag coefficient, but mostly empirical. The polynomial model is one the most commonly used as defined by

$$C_\mathrm{D} = a_1 + \frac{a_2}{Re} + \frac{a_3}{Re^2}, \tag{10}$$

where a_1, a_2, and a_3 are constants that apply for smooth particles over several ranges of Re [21].

The second term in Eq. (7) is the buoyancy force, which is important in simulating the sedimentation of solid particles in fluid, and the third term (F_i) represents a combination of additional forces in the particle force balance.

A particle trajectory is obtained by the solution of the particle momentum equation (Eq. (7)) coupled with the kinematic equation:

$$u_i^\mathrm{p} = \frac{\mathrm{d}x_i}{\mathrm{d}t}, \tag{11}$$

where x_i is the position coordinate of the particle at time t.

If there is a transfer of momentum from the particulate phase to the continuum phase, then the following computational approach is followed. The computed particle trajectories are combined into the source term of momentum, which is then inserted into the right-hand side of the conservation of the momentum equation:

$$\frac{\partial(\rho \bar{u}_j \bar{u})_i}{\partial x_j} + \rho \frac{\partial}{\partial x_j}(\rho \bar{u}'_i \bar{u}'_i) = -\frac{\partial \bar{p}}{\partial x_j} + \frac{\partial}{\partial x_j}\left[\mu\left(\frac{\partial \bar{u}_i}{\partial x_j} + \frac{\partial \bar{u}_j}{\partial x_i}\right)\right] + \Phi_i^M, \tag{12}$$

where $\Phi_i^M(C)$ is the source term. For each cell C, the source term is defined as

$$\Phi_i^M(C) = \frac{1}{V_\mathrm{C}} \sum_{j=1}^{n_\mathrm{C}} \eta_j \int_{\Delta t_j^\mathrm{C}} \frac{3\mu C_\mathrm{D}\, Re\, V_\mathrm{p}}{4 d_\mathrm{p}^2} (u_i - u_i^\mathrm{p})\, \mathrm{d}t, \tag{13}$$

where V_C is the volume of the cell, V_p is the volume of the particle, η_j is the number of particles per unit time traversing the jth trajectory, and Δt_j^C is the time that a particle on the jth trajectory takes to pass through cell C [22].

This two-way coupling is accomplished by alternatively solving the discrete and continuous phase equations until the solutions in both phases have stopped changing (i.e. until the convergence criteria are met).

4. Experimental investigation

A H13 tool steel atomized powder was used as the additive material in the LBDMD process to perform experiments with gas–powder flow. The size distribution of

Table 1
Size distribution of H13 tool steel powder for the experiment [23]

US standard mesh (powder size)	+80 (> 180 µm)	80/100 (180–150 µm)	100/140 (150–106 µm)	140/200 (106–75 µm)	200/270 (75–53 µm)	270/325 (53–45 µm)	325/D (> 45 µm)
Size analysis (%)	0	0.77	20.60	44.96	28.0	4.56	1.11

the powder is shown in Table 1. The powder was carried by the primary inert gas (Argon) at a flow rate of 0.354 m^3/h. Passing through the four 0.9-mm diameter nozzles, the mixture reached the speed of 37.1 m/s. The corresponding Reynolds number (*Re*) of 2300 indicates transitional flow in the nozzles. The total mass flow rate of the powder was 8 g/min, which represents a volumetric fraction of 0.034% in the stream. The secondary gas flowed from the coaxial nozzle at a volumetric flow rate of 0.354 m^3/h. The standoff distance measured from the top edge of the nozzle tips to the substrate was 4.75 mm. The gas–powder mixture flows along the thin wall buildup of the uniform thickness of 1.1 mm from the top to the bottom. The gas–powder flow was analyzed without laser–material interaction.

The representative cases in the process are: free gas–powder flow, gas–powder flow at the start of the deposition on the flat substrate, and gas–powder flow around the thin wall structure.

For this experimental investigation, digital imaging and analysis methods were selected, since they are non-intrusive and require no measuring equipment that could disturb the powder flow. This visualization technique was applied with a diode laser light source Lasiris™ with 660 nm wavelength. The laser light passed through a structured light projector in order to provide a 200-µm thick sheet of light with uniform (non-Gaussian) intensity distribution. The vertical sheet of light was projected through the powder cloud below the nozzle setup, and images were taken against a black background with a digital camera set to high resolution (Fig. 2a). For horizontal cross-sections of the powder cloud, the laser beam was projected horizontally, and the images were taken using a mirror set placed at 45° with respect to the horizontal plane (Fig. 2b).

5. Model description

The solution technique used in this study is based on the FLUENT software, which solves the conservation equations for mass and momentum by a specified finite-volume method [17]. The governing equations are discretized on a curvilinear grid to enable the computations in complex/irregular geometry.

The geometric domains and boundary conditions for simulated gas–powder structures in all representative cases are shown in Fig. 3. The structures are generated by a combination of the gas streams from the radially symmetrical primary nozzles and the coaxial secondary nozzle.

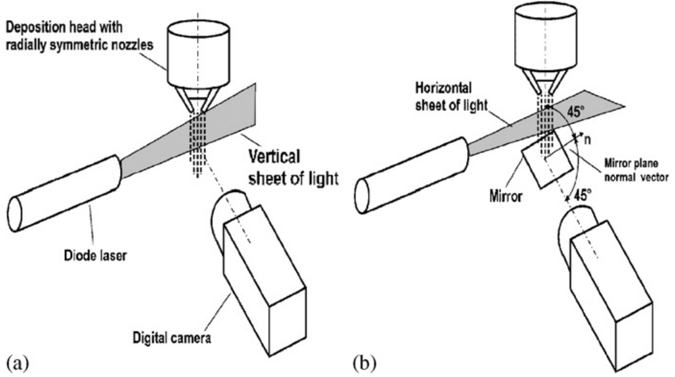

Fig. 2. Experimental setup for imaging of powder distribution in: (a) vertical cross-sections and (b) horizontal cross-sections.

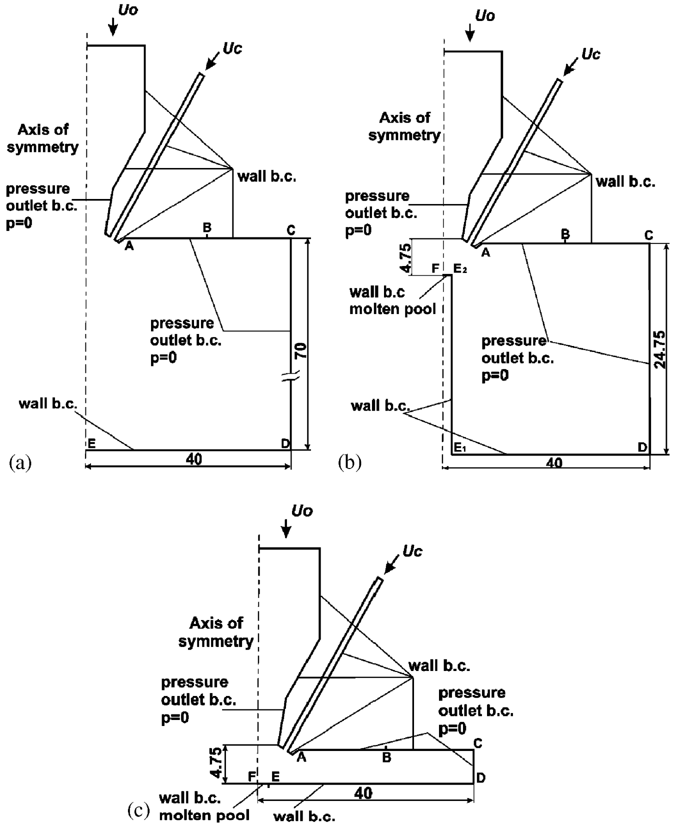

Fig. 3. Geometry and boundary conditions (cross-section) for analysis: (a) free gas–powder flow, (b) gas–powder flow around the thin wall, and (c) gas–powder flow at the start of the deposition on the flat substrate (u_c—carrier gas–powder velocity, u_o—optics protective gas velocity).

Metal powder is delivered by the stream at a carrier gas velocity u_p. The optics protective gas stream flows from the secondary nozzle at a velocity u_o. In all three cases, the computational domain consists of the four radially symmetrical nozzles, the coaxial nozzle, and the cylindrical area below the nozzles, which is large enough ($R = 40\,\mathrm{mm}$) to capture all the phenomena of interest. The cylindrical area is bounded by the wall boundary conditions at the substrate (ED), while the pressure outlet boundary condition ($p = 0$) is defined at the side (CD) and the top surfaces (AB). Since the part of the top surface, which is far from the axis of symmetry (BC), has little influence on the gas–powder flow below the nozzles, it is defined as a wall boundary condition to provide a better numerical stability of the solution. The area of the molten pool (FE) acts as a wall boundary condition for the gas. Also, it has the capability of capturing powder particles, which accounts for the powder fusion to the substrate when the molten pool is established. Since the computational domain has two plains of symmetry in the Cartesian coordinate system, it can be divided into four identical domains. Therefore, it is possible to solve the problem in only one of the quadrants by applying the appropriate boundary conditions on the planes of symmetry.

The grid selection is important to improve the accuracy of the solutions in most numerical simulation methods. There are two methods of grid generation that could be adopted in FLUENT software. For a simple geometry without an edge or curve, the Cartesian coordinate grid system might be used. Otherwise, the body fitted coordinate (BFC) grid system is used. In order to accurately predict the powder concentration distribution of the jet stream, the BFC grid system is used in this study. This allows the non-standard geometry of the nozzle to be mapped into Cartesian or cylindrical geometry [17]. The acceptability of the grid generation is checked automatically by the FLUENT software and is verified using the residuals list of the convergence in the computation.

The computational domains are discretized using GAMBIT software. Since the geometry is complex, a non-conformal mesh must be used. Therefore, the segments of the computational domain such as the nozzles and the major parts of the cylindrical area below the nozzles can be meshed by hexagonal cells; but, the part of the cylindrical area that is attached to the nozzles must be meshed by tetrahedral cells. To connect these zones, it is necessary to create interfaces between them. Fig. 4 shows the BFC grid selection for the zone where the nozzles are connected to the cylindrical area.

The following assumptions are taken during the jet flow simulation by FLUENT software:

- The jet flow problem is treated as a steady-state turbulent flow with a constant velocity distribution in the inlet boundary.
- Only the forces of drag, inertia, and gravity are considered in this study; other forces such as pressure and the surrounding flow acceleration are neglected.
- Since the powder particles volume fraction is less than 10% a dilute gas-particle stream is assumed. This assumption allows the application of one-way coupled discrete phase modeling.
- The effect of velocity fluctuation on a particle trajectory calculation is considered.
- The particle collision is not considered.
- The heat transfer by laser radiation is neglected.
- The particle size is assumed to follow the general Rossin–Rammler distribution expression [24].
- The molten pool is defined as a wall boundary condition with the ability to trap the particles while the pressure outlets ($p = 0$) let the particles escape.

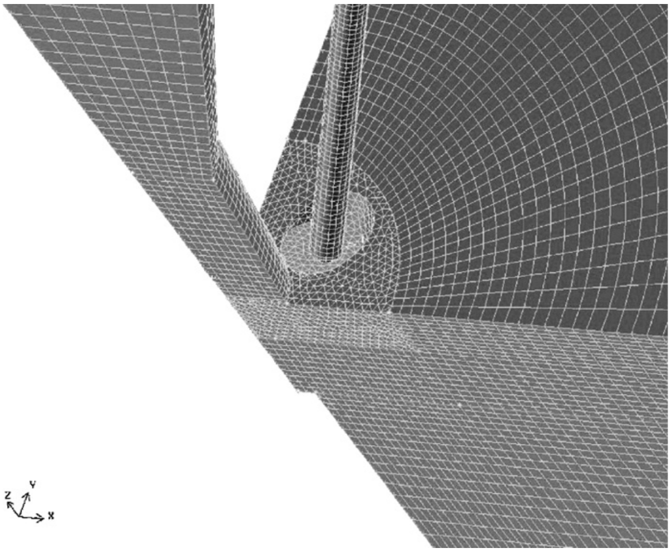

Fig. 4. Meshed geometry for flow analysis at the nozzles' connecting zone (first quadrant).

6. Results and discussion

The physical model of the compound jet with a dispersed powder was solved. The results are based on the different configurations in the three cases. Normally more than 300 numerical iterations are required for the first step (gas flow) to be solved in each simulation case. To solve the coupling problem of the gas and powder phases, 300 iterations (time steps of 0.0001 s) were assigned, which is long enough to follow the particles from the inlet to all domain boundaries.

The solution of the *free gas–powder flow* shows the turbulent nature in the area below the nozzles. The gas flow through the radially symmetric nozzles is transitional ($Re = 2300$) while in the area below the nozzles it becomes turbulent. The turbulence in this area causes an upward gas flow towards the coaxial nozzle and optics in the deposition head. This upward flow is not critical in the case when there is no laser–material interaction, since it does not consist of the metal fumes and ricocheted particles. However, this

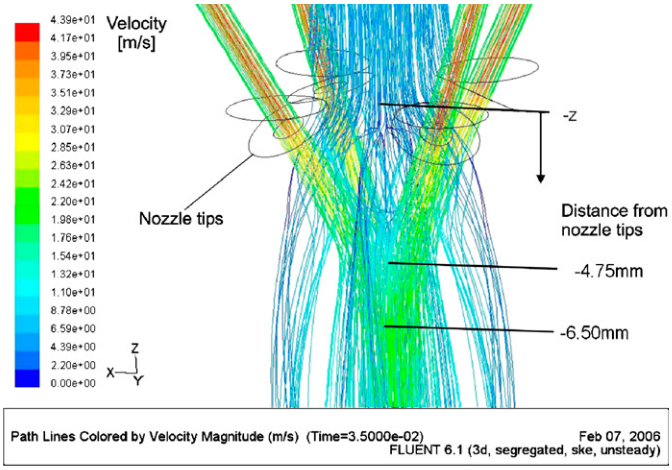

Fig. 5. Path lines of the gas free flow from the nozzles colored by velocity magnitude.

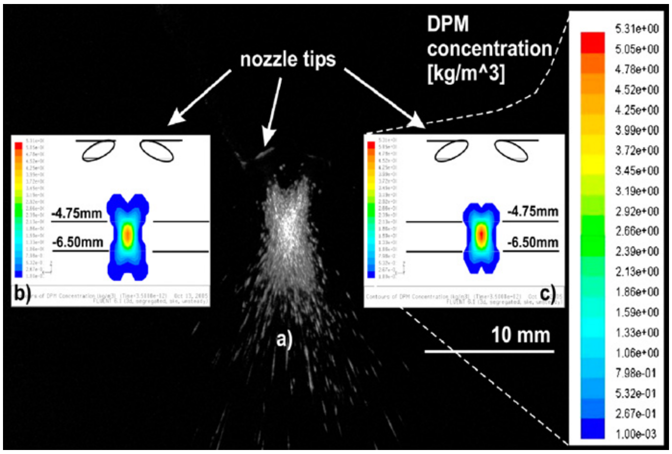

Fig. 6. Vertical cross-section of powder cloud below the nozzles: (a) digital image, (b) concentration contours from simulation in the plane 100 μm offset from the plane of symmetry, and (c) concentration contours in the plane of symmetry.

flow is blocked by the downward flow of the protective gas and redirected to the side open area between the powder feeding nozzles (Fig. 5).

The gas–powder mixture injected at the nozzle inlets reaches a fully developed flow while traveling through the nozzles. After they leave the nozzles, the four jets intersect with each other forming a cylindrical area of a maximum powder concentration along the vertical axis in the standoff distance range from −4.75 mm to −6.50 mm (Fig. 6).

Fig. 6a shows a digital image of the powder cloud cross-section below the nozzles where pixel gray level coresponds to powder concentration. Since the sheet of laser light projected through the cloud has a finite thickness of 200 μm, the image is slightly different from the concentration contours in the plane of symmetry (Fig. 6c), but it is in good agreement with the concentration contours in the plane 100 μm offset from the plane of symmetry. The comparison between the cloud image and numerically obtained powder concentration (see Fig. 6.) confirms the same location of the high powder concentration area. This is the zone where the substrate or molten pool is supposed to be in order to provide a high-quality deposition and high powder efficiency.

The curves of the powder concentration distribution in the horizontal planes at different distances from the nozzle outlets are presented in Fig. 7. It is shown that the largest powder concentration is distributed along the axis of symmetry, and it ranges from 2 to 5.31 kg/m^3 for the standoff distance from −4.75 to −6.50 mm.

After the gas–powder mixture leaves the nozzles, the gas flow starts to decelerate (Fig. 5). The powder particle streams driven by the inertia cross each other and form a powder cloud. Since there are few interparticle collisions in the cloud, the powder streams will keep traveling without changing their directions. Horizontal cross-sections of the powder flow streams are presented in Fig. 8, and their geometry is in good agreement with the results obtained by

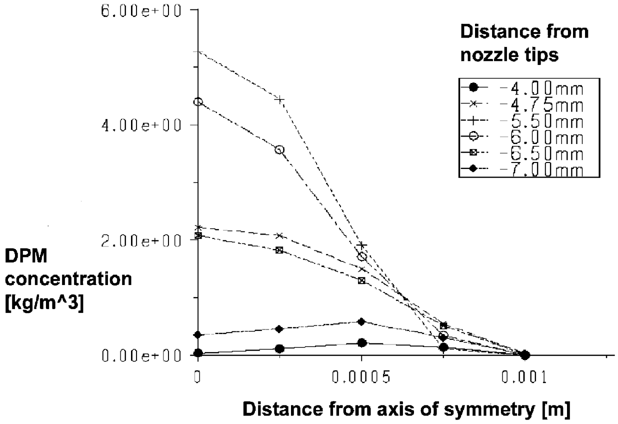

Fig. 7. Concentration distribution across the powder cloud.

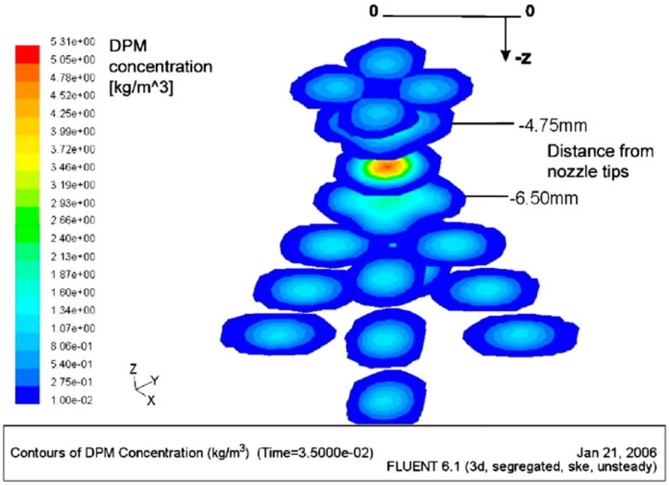

Fig. 8. Horizontal cross-sections (powder concentration) of the powder streams.

the processing of the corresponding images from the experiment (Fig. 9).

The analysis of the free flow shows that a 4.75-mm standoff distance represents the upper limit (Fig. 6) that will provide a coincidence of the powder cloud with the molten pool position for the best powder catchment efficiency. Due to the high turbulence intensity in the zone between the nozzles and substrate, the critical case for the process, regarding the optics protection and blob formation, is *the start of the deposition process* when the nozzles are at 4.75 mm above a flat and wide substrate.

The protective gas that flows from the coaxial nozzle effectively stops the upward directed fume and bouncing particles, forcing them to flow laterally among the powder nozzles. Also, the intense powder absorption in the molten pool can be observed in Fig. 10b. This is manifested by a lower powder concentration above the molten pool with respect to the powder concentration distribution in the case when the molten pool does not exist (Fig. 10a) and powder richochets intensively from the substrate.

The biggest concern regarding the process stability is the blob formation on the nozzle tips that blocks the gas–powder flow as well as the laser–substrate interaction. This phenomenon is more likely to occur when the nozzles are in close proximity to the substrate. The particles ricocheted from the substrate will hit the nozzle tips. Depending on the powder chemical composition and the size of the particles, some percentage of these particles stick to the nozzles. Also, the nozzle tips are exposed to the laser beam reflecton, especially at a higher laser power (above 400 W). These two unwanted side effects will cause a blob formation during the long-lasting deposition process on a flat surface. However, at a lower laser power, the ricocheted particles do not give cause for concern. Particle tracing during the simulation reveals a number of powder particles that hit the nozzle tips (Fig. 11). This is confirmed

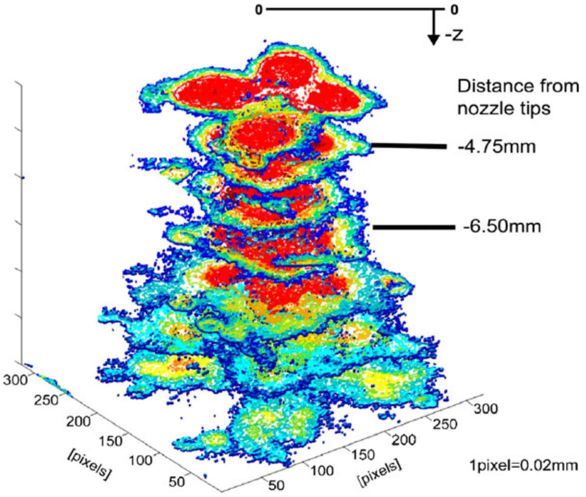

Fig. 9. Images of the powder flow horizontal cross-sections.

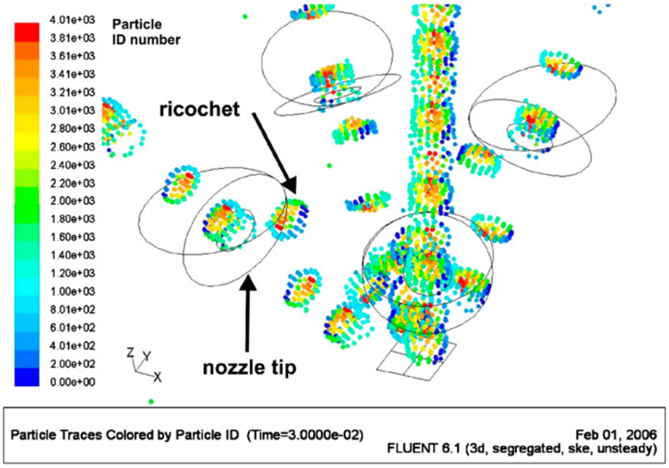

Fig. 11. Particle tracing in the simulation of the powder flow between the nozzles and flat substrate.

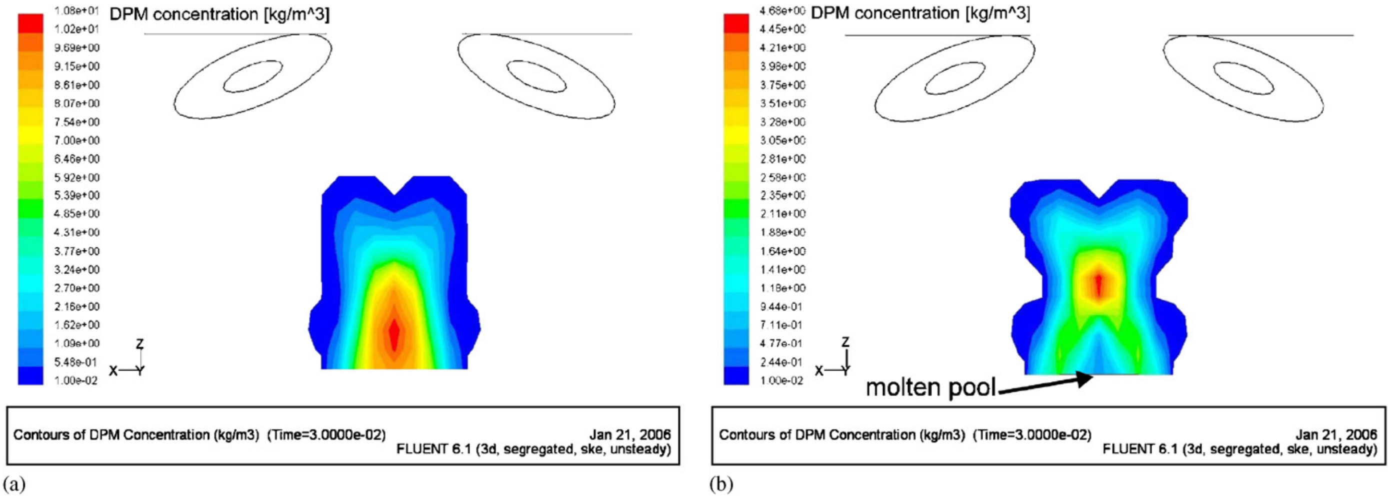

Fig. 10. Powder concentration contours in vertical plane of symmetry: (a) with molten pool and (b) without molten pool.

by imaging the powder cloud during the experiment (Fig. 12). Since it is not possible to take an image of the powder flow during the deposition when the laser interacts with the substrate and the powder, the comparison is performed for the case when the laser is off (the molten pool is not generated).

Finally, the gas–powder *flow around the thin wall* has been analyzed. A model has been developed for a standoff distance of 4.75 mm, and the modeling results of the powder flow concentration with and without a molten pool is shown in Fig. 13. A lower concentration of the ricocheted powder is observed in the area between the molten pool and the nozzles than in the previous case. It means that some of non-fused particles will bounce from the side of the wall towards the substrate; so fewer particles hit the nozzle tips. Also, the smaller and non-flat area of the substrate causes less of a laser beam reflection towards the nozzle tips. As a consequence, the blob formation during the wall deposition has never been observed. Fig. 14 presents an image of the powder flow in the deposition head vertical plane of symmetry. The wall is shown in frontal view (see Fig. 14), and only the left half of the powder flow below the top of the wall is visible since the wall blocks the sheet of laser light.

According to the free gas–powder flow analysis, the standoff distance in the range from 4.75 to 6.50 mm should provide a high-powder efficiency, as well as a stable deposition process that will reflect in making an accurate buildup geometry. The verification of the numerical simulation results is performed by building the straight thin wall at different standoff distances. For the standoff distance between 4.75 and 6.50 mm, the wall is successfully built with an accurate height (Fig. 15a). The wall thickness is slightly varying as a consequence of the laser beam diameter variation with the change of standoff distance. During the experiments with a standoff distance less than 4.75 mm, the process becomes unstable because of the restricted powder delivery in the vertical plane. In this case,

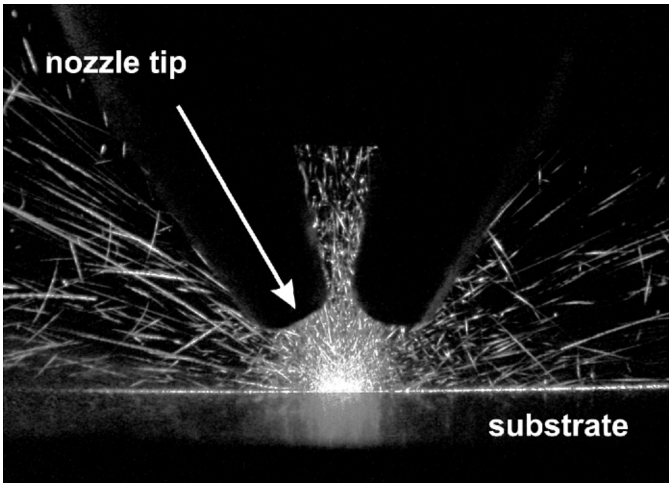

Fig. 12. Image of the powder flow between the nozzles and flat substrate (deposition head vertical plane of symmetry).

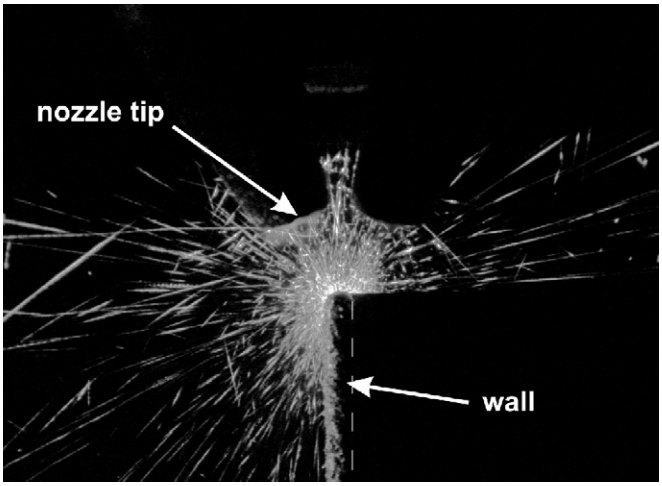

Fig. 14. Image of the powder flow between the nozzles and thin-walled structure (nozzles' vertical plane of symmetry perpendicular to the wall).

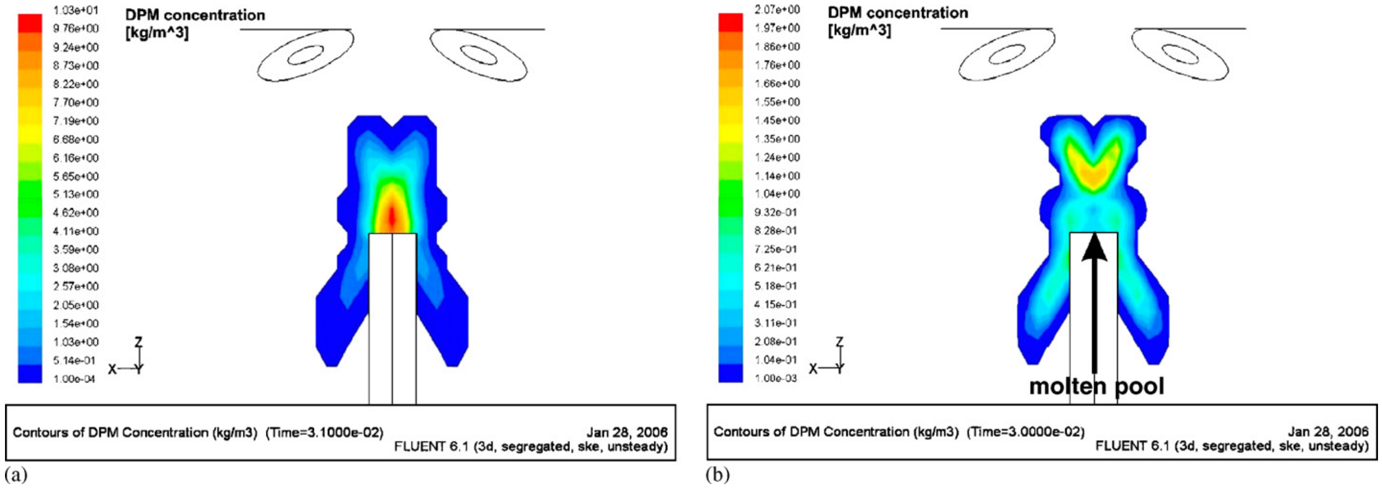

Fig. 13. Powder concentration contours in vertical plane of symmetry: (a) without molten pool and (b) with molten pool.

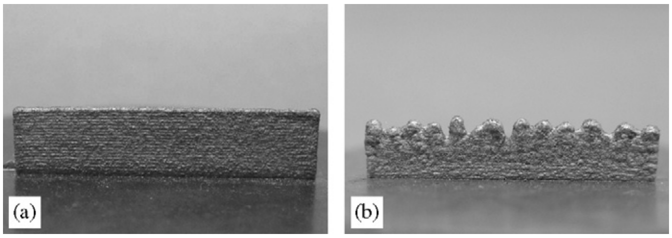

Fig. 15. Buildup geometry deposited with (a) standoff distance from 4.75 to 6.50 mm and (b) with standoff distance less than 4.75 mm.

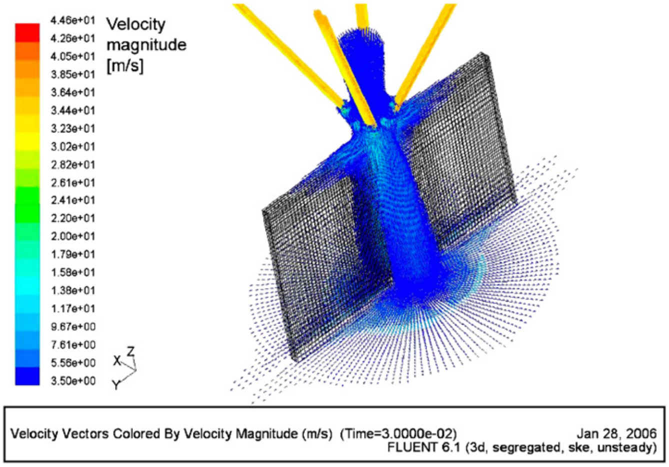

Fig. 16. Gas velocity vectors around the wall.

ripples on the top edge of the wall will be formed. Furthermore, the laser beam becomes defocused along the top edge of the wall, and the geometrical error propagates as the deposition continues. In this case, the required wall geometry is not achieved (Fig. 15b). This is in good agreement with the results from Fearon et al. [8], where they investigated the influence of the powder stream geometry on the process stability and the deposited layer height.

The model of gas–powder flow around the wall has been developed as a complementary model to the thermo-structural FEM of the LBDMD of thin-walled structures that has been developed by the authors of this paper [14]. The distribution of the gas velocity around the wall was used to calculate the correct boundary conditions for the heat transfer model. The model reveals zones of intense gas flow over the wall surfaces (Fig. 16). These areas are exposed to forced convection, and the coefficient of heat transfer between the wall and the surrounding area can be calculated using the gas velocity values obtained from the gas flow analysis.

7. Conclusions

The results discussed in this paper seek to address some powder delivery issues associated with the laser-based direct metal deposition. The potential of the process numerical modeling combined with the experimental results is used as a powerful tool to obtain a better understanding of the phenomena observed during the direct laser metal deposition, and to analyze the influence of the gas–powder flow characteristics on the process stability and the process output. A 3D discrete phase model of the gas–powder flow in the LBDMD process has been developed using FLUENT numerical software.

The significant findings derived from this work are summarized below:

(a) Since the particle volume fraction of the powder in the gas flow is less than 10% (0.034%), a discrete phase model is used to simulate the process.
(b) The analysis proved the importance of the secondary gas flow for laser head optics protection especially in the deposition process over flat surfaces where turbulence and particle ricochet is more pronounced.
(c) Also, the theory that the blob formation at the nozzle tips is a result of the ricocheted powder particles impacting the nozzle tips is proven.
(d) The powder flow pattern after the nozzle outlet is slightly different from the gas flow. The powder concentration distribution reveals that the standoff distance in a specific range can provide a stable powder delivery and accurate buildup geometry, which is in agreement with the experimental results.
(e) The gas flow model around the wall, as a complementary model to the thermo-structural FEM of laser metal deposition, provides important data for the calculations of the boundary conditions in the heat transfer model.

Acknowledgements

This work was financially supported by the National Science Foundation Grant No. DMI-03200663. The authors would like to acknowledge Mr. Michael Valant, research engineer at the Research Center for Advanced Manufacturing, Southern Methodist University, for his contribution in the experimental part of this work.

References

[1] J. Mazumder, D. Dutta, A. Ghosh, N. Kikuchi, Designed materials: what and how, Proceedings of the SPIE 4831 (2003) 505–516.
[2] T. Wohlers, Wohlers Report—Rapid Prototyping, Tooling & Manufacturing State of the Industry, Wohlers Associates Inc., Colorado, 2003.
[3] V. Malin, R.N. Johnson, F. Sciammarella, Laser cladding helps refurbish US Navy ship components, The AMPTIAC Quarterly 8 (3) (2005) 3–9.
[4] P.A. Vetter, T. Engel, J. Fontaine, Laser cladding: the relevant parameters for process control, Proceedings of the Laser Materials Processing: Industrial and Microelectronics Applications SPIE 2207 (1994) 452–462.
[5] A. Weisheit, G. Backes, R. Stromeyer, A. Gasser, K. Wissenbach, R. Poprawe, Powder injection: the key to reconditioning and generating

components using laser cladding, Proceedings of International Congress on Advanced Materials and Processes, Materials Week 2001, Munich, Germany, October 2001.

[6] R. Kovacevic, System and method for fabrication or repairing part, Accepted US Patent Application No. 10/649,925, 2005.

[7] M. Valant, R. Kovacevic, Powder delivery System, Accepted US Patent Application No. 10/648,554, 2005.

[8] E. Fearon, K.G. Watkins, Optimization of layer height control in direct laser deposition, Proceedings of the 23rd International Congress on Applications of Laser and Electro-optics (ICALEO 2004), San Francisco, CA, 03–07 October 2004.

[9] J. Lin, Laser attenuation of the focused powder streams in coaxial laser cladding, Journal of Laser Applications 12 (1) (2000) 28–33.

[10] A.J. Pinkerton, L. Lin, Modelling powder concentration distribution from a coaxial deposition nozzle for laser-based rapid tooling, Journal of Manufacturing Science and Engineering, ASME 126 (2004) 33–41.

[11] S. Levy, Two-Phase Flow in Complex Systems, Wiley, New York, 2000.

[12] J. Lin, Numerical simulation of the focused powder streams in coaxial laser cladding, Journal of Materials Processing Technology 105 (2000) 17–23.

[13] F.W. Liou, J. Ruan, H. Pan, L. Han, M.R. Boddu, A multi-axis hybrid manufacturing process, 2004 NSF Design, Service and Manufacturing Grantees and Research Conference/SMU, Dallas, TX, January 2004.

[14] S. Zekovic, R. Dwivedi, R. Kovacevic, Thermo-structural finite element analysis of direct laser metal deposited thin-walled structures, Proceedings of the SFF Symposium, Austin, TX, August 2005.

[15] N. Rajaratnam, Turbulent Jets, Elsevier, Amsterdam, 1976.

[16] B.E. Launder, D.B. Spalding, Lectures in Mathematical Models of Turbulence, Academics Press, London, England, 1972.

[17] Fluent Inc., FLUENT 6.2.1 User Guide, 2004.

[18] R.A. Antonia, R.W. Bilger, An experimental investigation of an axisymmetric jet in co-flowing air stream, Journal of Fluid Mechanics 61 (1973) 805–822.

[19] V.L. Streeter, Handbook of Fluid Dynamics, McGraw-Hill, New York, 1961.

[20] C.T. Crowe, Review—numerical models for dilute gas-particle flows, ASME Transactions, Journal of Fluid Engineering 104 (1982) 297–303.

[21] S.A. Morsi, A.J. Alexander, An investigation of particle trajectories in two-phase flow systems, Journal of Fluid Mechanics 55 (2) (1972) 193–208.

[22] K. Babets, Numerical modeling and optimization of waterjet based surface decontamination, Ph.D. Thesis, The New Jersey Institute of Technology, 2001.

[23] J. Choi, Y. Hua, Dimensional and material characteristics of direct deposited H13 tool steel by CO_2 laser, Journal of Laser Applications 16 (4) (2004) 245–251.

[24] J. Fan, H. Zhao, K. Chen, An experimental study of two-phase turbulent coaxial jets, Experiments in Fluids 13 (1992) 279–287.